ROYAL SOCIETY OF CHEMISTRY

EDGE ARTICLE

Check for updates

All publication charges for this article have been paid for by the Royal Society of Chemistry

Engineering copper plasmonic chirality *via* ligand-induced dissolution for enantioselective recognition of amino acids†

Sonia Maniappan,[a] Camelia Dutta,[a] Arunima Cheran,[a] Diego M. Solís[b] and Jatish Kumar [iD] *[a]

The formation of chiral nanosystems and their subsequent enantioselective interaction with chiral amino acids are vital steps in many biological processes. Due to their potential to mimic biological systems, the synthesis of chiral nanomaterials has garnered significant attention over the years. Despite the emergence of diverse nanomaterials showcasing strong chiral responses, the in-depth understanding of the mechanism of plasmonic chirality in copper nanoparticles and their subsequent application in various fields are least explored. Herein, we demonstrate a facile approach for the synthesis of chiral copper nanoparticles using cysteine as a chiral precursor and capping ligand. Ligand-mediated chiral induction, established through experimental findings and a theoretical model, is ascribed as the major contributor to the origin of plasmonic chirality. The enantioselective recognition of chiral copper nanoparticles towards histidine, an amino acid with vast biological functions, was meticulously investigated by leveraging the strong copper–histidine binding ability. Ligand-induced dissolution, a unique phenomenon in nanoparticle reactions, was identified as the underlying mechanism for the nanoparticle-to-complex conversion. Understanding the mechanism of chiral induction in copper nanoparticles coupled with their enantioselective recognition of biomolecules not only holds promise in biomedical research but also sheds light on their potential as catalysts for asymmetric synthesis.

Introduction

Investigations on chiral nanomaterials have been marked as an inevitable domain over the past few years, not restricted to their significance to the origin of homochirality but also due to their relevance in the field of chiral sensors, asymmetric catalysis, and metamaterials in advanced optical devices.[1–6] Strong chiral responses are reported from various materials comprising metal nanoparticles, semiconductor quantum dots, nanocarbon and hybrid nanomaterials.[7–10] There has been a recent surge in the fabrication of versatile nanomaterials with diverse chiral morphologies, owing to advancements in bottom-up strategies developed for the tailored synthesis of nanostructures.[11–16] Of special interest are chiral metal nanoparticles that exhibit localized surface plasmon resonance (LSPR), the collective oscillation of electrons upon interaction with electromagnetic radiation. LSPR enables focusing of light onto nano-dimensions

and endows the particles with exceptional optical properties in visible and near-infrared regions.[17–21] The optical activity in plasmonic nanomaterials is governed by different origins that include (i) structural distortion induced by chiral ligands during nanoparticle synthesis, (ii) assembly of achiral nanoparticles in the presence of chiral templates, and (iii) induced chirality through the hybridization of the electronic states of nanoparticles and chiral ligands.[22–24]

The generation of chirality and its intriguing applications are well explored in plasmonic nanomaterials, such as gold and silver.[25–27] However, the fundamental understanding and applicability of chiral copper nanoparticles (CuNPs) is an area that remains underdeveloped. Owing to their excellent electrical and thermal properties, comprehended by their unique optical response in the visible and near-infrared regions, copper nanomaterials that are relatively inexpensive are emerging as viable alternatives to precious metals like gold and silver in various plasmonic applications.[28–32] Despite their advantages, the synthesis of robust copper-based nanomaterials has remained a challenging task due to the low standard redox potential of the metal leading to surface passivation through formation of oxides.[33,34] In this context, dedicated efforts to develop facile strategies for the synthesis of stable CuNPs using appropriate capping ligands are a pressing priority.[35,36] While there are a few recent reports on the synthesis and chiroptical investigations of CuNPs, the existing

[a]Department of Chemistry Indian Institute of Science Education and Research (IISER) Tirupati, Tirupati 517507, India. E-mail: jatish@iisertirupati.ac.in

[b]Departamento de Tecnología de los Computadores y de las Comunicaciones, University of Extremadura, 10003 Cáceres, Spain

† Electronic supplementary information (ESI) available. CCDC 2308273 and 2308274. For ESI and crystallographic data in CIF or other electronic format see DOI: https://doi.org/10.1039/d4sc00477a

literature on this topic remains relatively limited, and comprehensive studies are required to fully understand the origin of chirality and to further explore their potential applications.[37–40] Herein, we establish a straightforward and efficient method to generate CuNPs from amino acids as a chiral precursor and capping agent. The optical activity of synthesized CuNPs was confirmed by circular dichroism (CD), which gave mirror image signals for the particles synthesized using L- and D-cysteine.

Furthermore, the major focus of investigations has been the enantioselective recognition of optically active CuNPs towards histidine. Histidine is a vital amino acid that is crucial for human growth and development as it serves as the precursor for histamine, which is essential for triggering inflammatory responses in the body. Histidine plays an important role in many biological functions like immune responses and is present in the active site of many metallozymes.[41,42] The significance of histidine extends beyond biological functions. It has proven useful in asymmetric synthesis and has been utilized as a catalyst for cross-aldol reactions involving enolizable aldehydes.[43] Unlike L-histidine, which is included in food supplements in the form of capsules, tablets, or injections, D-histidine does not have any functional role in the body, rendering the enantioselective recognition of histidine imperative.[44] Therefore, investigating the enantioselective interaction between chiral CuNPs and biomolecules, such as histidine, is of considerable interest in various biomedical applications. Taking advantage of strong Cu–histidine binding ability, the enantioselective interaction of the CuNPs with histidine was investigated, and the ligand-induced transformation of the CuNPs into metal complexes was probed. To the best of our knowledge, this is the first attempt toward using chiral CuNPs for establishing the enantioselective recognition of a specific amino acid.

Results and discussion

CuNPs were synthesized adopting a bottom-up approach using cysteine, a thiol-containing amino acid, as the capping ligand.

The optimized conditions which resulted in uniform CuNPs with intense optical activity involved the use of $CuCl_2 \cdot 2H_2O$, L-cysteine, and NaOH at concentrations of 10 mM, 10 mM, and 5 mM, respectively. Copper ions and L-cysteine react in alkaline solution, resulting in the formation of Cys–Cu–Cys mercaptide molecules through Cu–S coordination. As the concentration increases, water-insoluble Cys–Cu–Cys molecules progressively self-assemble giving rise to the formation of CuNPs.[45] The morphology of the CuNPs investigated using transmission electron microscopy (TEM) (Fig. 1a and b) and atomic force microscopy (AFM) (Fig. 1c and S1†) showed the formation of roughly spherical particles with an average size of 58.2 ± 8.5 nm. TEM images displayed interconnected particles, likely to be formed during drying on the grid (Fig. S2†). The lattice parameters and crystallinity were studied using powder X-ray diffraction (PXRD) measurements. The PXRD pattern exhibited well-defined peaks at 2θ values of 29.8°, 42.86°, 52.98°, 60.2°, and 69.72°, which can be ascribed to crystallographic planes (110), (200), (211), (220), and (311), respectively, of Cu_2O nanoparticles (Fig. 1d).[46] Nevertheless, there were also minor peaks indicative of a trace presence of metallic Cu and CuO.[47] The valence states of the synthesized particles determined using X-ray photoelectron spectroscopy (XPS) showed peaks with binding energies at 936.2 and 955.9 eV, which correspond to Cu $2p_{3/2}$ and Cu $2p_{1/2}$ (Fig. 1f) respectively. The satellite peak at 947 eV is attributed to the binding energy from the open $3d^9$ shell of Cu(I) oxidation state.[48] The survey scan of the XPS analysis shows that the synthesized nanoparticles are composed of C (1s), O (1s), N (1s), and S (2p) (Fig. S3 and Table S1†). The investigation of functional groups on the synthesized CuNPs was accomplished through FT-IR analysis. The absence of peaks at 2552 and 931 cm^{-1} corresponding to the S–H stretching vibrations of L-cysteine suggests the formation of Cu–cysteine bond *via* thiolate interaction (Fig. 1e). The band for carboxylate stretching in the free cysteine molecule, typically observed at 1770–1690 cm^{-1}, undergoes a shift suggesting the involvement of the acidic group in hydrogen bonding
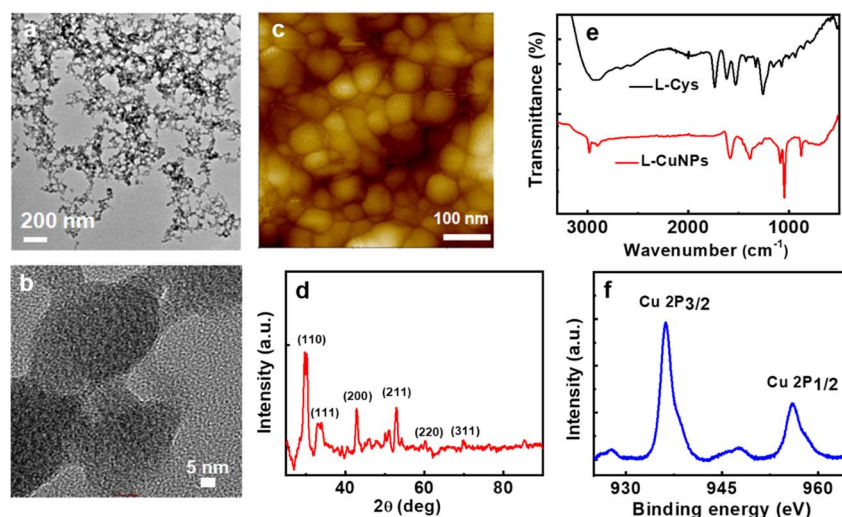

Fig. 1 TEM images at (a) low and (b) high magnifications, (c) AFM image, and (d) PXRD pattern of L-CuNPs. (e) FTIR spectra of L-cysteine (black trace) and CuNPs synthesized using L-cysteine (red trace). (f) Cu 2p XPS spectrum of CuNPs synthesised in the presence L-cysteine.

interactions with other neighboring cysteine molecules on the CuNP surface.[49] The Raman spectral analysis of L-CuNPs revealed prominent peaks at 253 and 500 cm^{-1}, attributed to Cu–S and S–S bonds present in excess cysteine (Fig. S4†).[50] Furthermore, Raman signals observed at 215, 500, and 640 cm^{-1} are associated with the second-order overtone mode 2Eu, Raman-allowed mode F_{2g} and Raman-allowed mode TO, respectively, for Cu_2O.[51]

The optical properties of the synthesized CuNPs were analyzed using UV-visible and CD spectroscopy. The UV-visible spectra showed typical features in the region corresponding to the LSPR and interband transition of CuNPs: a broad absorption peak covering 500–800 nm with a shoulder at around 620 nm (Fig. 2a). The nanoparticles showed mirror image CD spectra for the particles synthesized using opposite enantiomers of the amino acid with a g_{abs} value of -1.1×10^{-3} and 1.21×10^{-3} (at 613 nm) for L- and D-CuNPs, respectively (Fig. 2b). Positive and negative couplets were observed for the nanoparticles synthesized using L- and D-cysteine, respectively. CD signals observed in the visible and NIR region of the electromagnetic spectrum must originate from the interactions of the CuNPs with the chiral field of the ligand.[52] The stability of the CuNPs was assessed by monitoring spectral changes over a period of several days. The consistency in the position and intensity of the absorption and CD peaks revealed that the nanoparticles remained stable without any degradation over the entire period of analysis (Fig. S5†). Moreover, the stability of the CuNPs was evaluated in solvents of varying polarity. Among different solvents analyzed, nanoparticles dispersed in polar solvents, such as water, ethanol, and DMSO, were found to retain their spectral profile confirming their stability in these solvents (Fig. S6†). The pH-dependent stability analysis revealed that at lower pH the CuNPs exhibited a broadened UV-visible signal and weak CD due to the aggregation of cysteine (Fig. S7†).[53] Notably, the CuNPs displayed relatively high stability at pH 9 due to the absence of electrostatic interaction between the uncharged amino group and negatively charged carboxylic group, thus preventing their aggregation.[54] To demonstrate the optical properties of the synthesized nanoparticles in the solid state, self-standing films of the CuNPs in polyvinyl alcohol (PVA) were fabricated. CD plots of transparent polymeric films exhibited spectral signatures similar to those in solution, albeit with a slight broadening (Fig. S8†) pointing to the applicability of the nanoparticles as optically active solid-state material. Moreover, incorporation in a polymer matrix can be adopted as a viable strategy to protect the particles from surface oxidation.

To further understand the physical origin and nuances of chirality in our synthesized CuNPs, a theoretical analysis was carried out: the roughly spherical shape of these shells justifies the assumption of two ideally spherical surfaces as interfaces separating the copper core, cysteine layer and water background. This allows for a completely analytical and exact solution to Maxwell's equations based on an expansion of vector spherical harmonics (Mie theory), with no approximations other than the above-mentioned assumption of perfect sphericity.[55] In Fig. 3, we apply this model to a single Cu sphere of radius 29.1 nm, surrounded by a 2 nm-thick cysteine coating with isotropic chiroptical activity (details on its parameterization can be found in the ESI†). Fig. 3a shows the extinction efficiency Q_e (in terms of extinction cross section divided by area: ECS/πr^2) vs. wavelength for incident L- (solid lines) and R-handed (dashed lines) plane-wave circular polarizations, considering different Cu-to-Cys volume fractions $f_{(Cu/Cys)}$. These curves are consistent with the experimental observation of a damped resonance around 600 nm: in the theoretical model, a sharper resonance emerges at 583 nm, together with an additional peak that redshifts as $f_{(Cu/Cys)}$ increases. Importantly, the first resonance not only is invariant with the Cu core radius, but it also shows up without the cysteine layer (see panels (c) and (d) of Fig. S9 of the ESI,† respectively); these findings, together with the isotropic nature of the sphere, lead us to conclude that the 583 nm resonance is mainly due to the interband transitions of copper, which rule its dielectric function for wavelengths below approximately 600 nm (above this threshold, a simple Drude model is sufficient to describe its metallic response, as shown in Fig. S9a†). As for the $f_{(Cu/Cys)}$-dependent peak, this can be tracked down to the 225 nm resonance of the model chosen for the permittivity of cysteine[56] (Fig. S9b†): in the effective medium approach, $f_{(Cu/Cys)}$ thus acts as a controlling factor that brings the position of this resonance to longer wavelengths. In Fig. 3a, there is a clear resonance splitting, e.g. for $f_{(Cu/Cys)} = 0.35$, but somewhere in the range [0.20, 0.30] (blue, red, green) these two modes become hybridized, which can already explain by itself, to some extent, the smoothed out experimental peak. This hybridization mechanism adds to the zero average anisotropies and Gaussian size distribution of synthesized quasi-spherical particles (polydispersity), which all contribute to this smoothing.

The monotonically increasing trend of the extinction towards higher energies observed in experimental measurements is not entirely present in these analytical results. Part of this discrepancy might be attributed to the absence of polydispersity in the theoretical model but, given the lack of anisotropy—at least in an average sense—and the above-
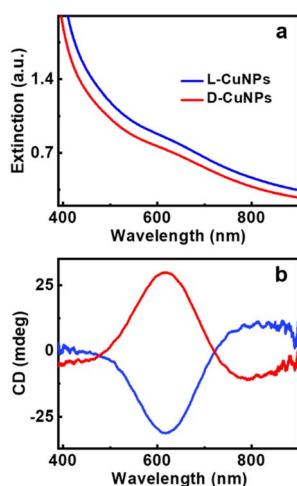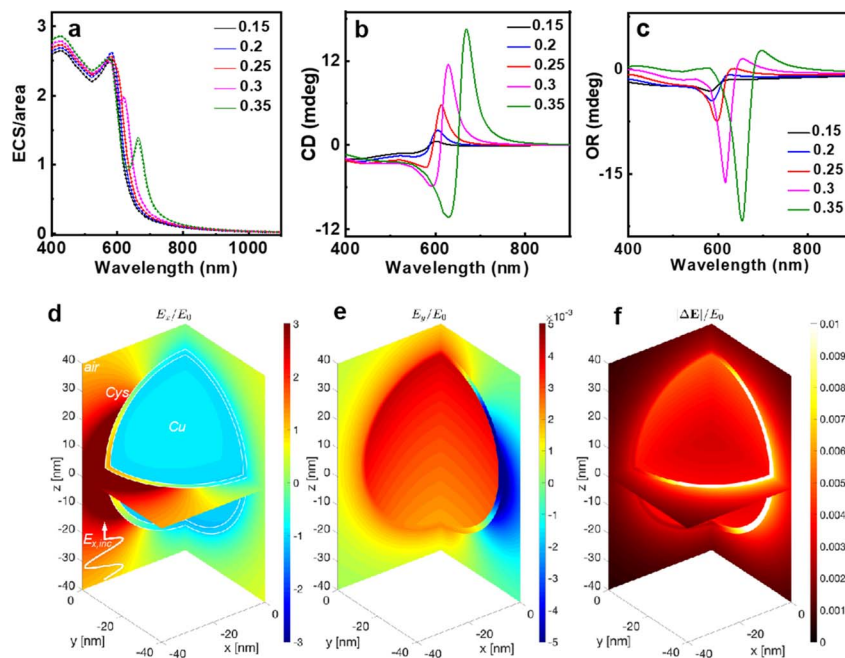

Fig. 2 (a) Extinction and (b) CD spectra of CuNPs synthesized using L-cysteine (blue trace) and D-cysteine (red trace) as capping ligands.

Fig. 3 Mie results of extinction and chiral response for a perfectly spherical CuNP with a 2 nm thick cysteine shell. (a) Extinction efficiency *vs.* wavelength, for several Cu-to-Cys volume fractions. (b) CD and (c) optical rotation of a 1 μm water slab with 5% in volume of dispersed CuNPs. (d, e) Colourmaps of the normalized total (*i.e.* incident plus scattered) electric field components E_x and E_y under *x*-polarized plane-wave illumination (incident field $\tilde{E}_{inc} = E_{inc}e^{i\omega t}$, with phasor $E_{inc} = \hat{x}E_0 e^{-i\frac{\omega}{c}z}$, $\omega = \frac{2\pi c}{\lambda}$ being the angular frequency and *c* the velocity of light) at 614 nm and $f_{(Cu/Cys)} = 0.25$ (coinciding with a maximum of CD in panel (b)), at planes $x = 0$ and $y = 0$ and assuming the spherical core−shell is centered at the coordinate origin. (f) Normalized norm of the electric-field phasor difference between chiral and nonchiral responses.

mentioned invariance of the extinction profile shape with particle size, it most likely can be related to slight divergences in the effective dielectric function of the synthesized copper with respect to tabulated values in ref. 57 in the region where interband transitions become preponderant, and/or some effective dielectric mixing of (Cu–Cys)/H$_2$O compounds.[57] This rationale is supported by the fact that, by replacing water with air as the background, extinction curves do match measurements in this low-wavelength region (Fig. S9c†): now, we stress, again, that the shape of the extinction curve is independent of the particle size, and hence, we would obtain similar curves by varying the dielectric function of copper such that $\varepsilon_{(Cu,new)}/\varepsilon_{water}\varepsilon \approx \varepsilon_{Cu}/\varepsilon_{air}$ within this high-energy region. In the framework of a Lorentzian model, a similar effect would be achieved in this case by simply reducing the value of the dielectric function by a small constant, *i.e.*, using a smaller effective ε_∞.

Fig. 3b and (c) show the quantification of chiroptical responses from L-CuNPs and how the results of approximations considered (see the ESI†), with variations of the order of ∼10 millidegrees in the [600–700] wavelength span, agree very well with the experimental measurements. Fig. 3d–(f) present near-field electric field distributions of a single CuNP at 614 nm, an operating point which in Fig. 3b (red curve) shows a maximum in CD when $f_{(Cu/Cys)} = 0.25$. Fig. 3d depicts the normalized E_x component—the real part of its phasor, to be more precise—when the incident field is polarized along the *x* axis with arbitrary magnitude E_0. In such a case, a chirally inactive sphere would produce identically zero E_y field

component at planes $x = 0$ and $y = 0$. Our chiral NP, however, yields normalized E_y values of ∼0.01, as shown in Fig. 3e. Fig. 3f illustrates the norm of the difference of (E_x, E_y, and E_z) electric field vectors with and without chiral response $\varepsilon_{Cys} = (\varepsilon_L + \varepsilon_R)/2$, which is basically the square root of the optical intensity of such a difference, again normalized to E_0. This colour map distinctly shows how the largest magnitudes happen inside the cysteine shell, as expected.

Establishment of the chiral nature of the synthesized CuNPs lays the groundwork for their application in enantioselective recognition. The enantioselective detection of amino acids by L-CuNPs was studied by the sequential addition of amino acids and monitoring the spectral changes. The addition of most amino acids to the CuNPs resulted in minimal/no noticeable changes in CuNP spectra. Interestingly, the addition of L-histidine to L-CuNPs resulted in distinct CD spectral profile; an inversion of the CD signal from a negative peak at 621 nm to a positive peak at 687 nm was the noted signature upon the interaction of L-histidine with L-CuNPs (Fig. 4b). The CD peak maxima displayed a remarkable bathochromic shift of 66 nm with an inversion of sign. In contrast, the addition of D-histidine to L-CuNPs resulted in an increase in the negative CD intensity with a bathochromic shift in peak position (Fig. 4d). The CD spectra after the reaction of L- and D-histidine with L-CuNPs showed mirror image spectral profiles (Fig. 5b). A similar pattern of CD peak reversal was observed with the addition of D-histidine to D-CuNPs (Fig. S10†). Hence, CD spectral changes observed in optically active CuNPs upon the addition of histidine could help
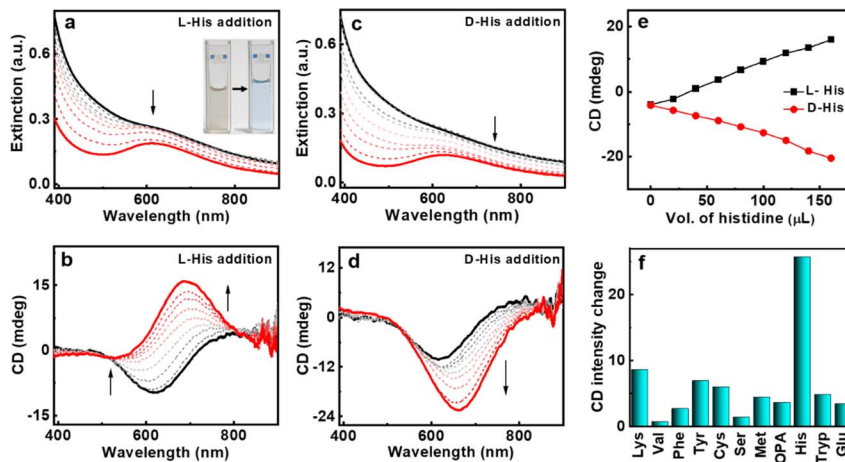
Fig. 4 (a, c) Extinction and (b, d) CD spectral changes of L-CuNPs upon the addition of (a, b) L-histidine and (c, d) D-histidine. (e) Plot depicting the variation of CD intensity monitored at 688 nm on stepwise addition of D- (red trace) and L-histidine (black trace) to L-CuNPs (final histidine conc. = 3.7 mM). (f) CD intensity plot of L-CuNPs on addition of different amino acids. Inset in (a) shows a photographic image of L-CuNPs before (left) and after (right) addition of histidine.

distinctly differentiate one enantiomer of histidine from the other (Fig. 4e). However, the introduction of a racemic mixture of histidine led to the disappearance of optical activity of CuNPs (Fig. S11†). In all cases, UV-visible spectra showed the conversion of the dampened band of CuNPs to a relatively structured peak upon interaction with L-histidine (Fig. 4a and c). The spectral changes were accompanied by a visual colour change of the solution from turbid brown to clear blue (inset, Fig. 4a). The studies with other sets of amino acids revealed that the spectral changes are minimal, highlighting the specificity of the CuNP interaction with histidine (Fig. 4f and S12–S14†). The optical measurements reveal that the synthesized chiral CuNPs can be used for selective identification of histidine as well as for its enantioselective recognition. The nature of the metal aids the selectivity towards amino acid (histidine), whereas nanoscale chirality helps in enantioselectivity.

The spectral changes observed during the addition of histidine to the CuNPs point towards a substantial change to the nanoparticles during the interaction. To further probe the changes occurring at the molecular level, the solution after the addition of histidine was purified and left undisturbed. To our surprise, crystal formation was observed over time. The formation of single crystals helped authenticate the molecular

structure using single-crystal X-ray diffraction (SC-XRD). Interestingly, SC-XRD data showed the formation of metal complexes that crystallized in monoclinic space groups (Fig. 5a and Table S2†). The crystal structure of the complex revealed a distorted square planar geometry with a Schiff base ligand formed from histidine (Fig. 5a).[58] The formation of the Schiff base ligand was facilitated by the self-aldol condensation of acetone, which occurred through a vapour diffusion process. In the observed structure, one copper atom is bound to two histidine ligands, each through a bidentate binding. One histidine, acting as negatively charged bidentate ligand, binds to the copper(II) center through N (amino) and O (carboxyl) atoms with bond lengths of 1.96 Å and 1.98 Å, respectively. The other histidine coordinates with the copper(II) center utilizing its amino and imidazole nitrogen atoms with bond lengths of 2.02 Å and 1.98 Å. The UV-visible and CD patterns observed during the addition of histidine to the CuNPs closely align with the expected spectral changes during the nanoparticle-to-complex conversion (*vide supra*). The addition of L- and D-histidine to the CuNPs resulted in opposite spectral features, indicating the conversion of nanoparticles to complexes with opposite handedness (Fig. 5b). The absorption band for the complex is the result of d–d transitions from the Cu^{2+} center.[59]
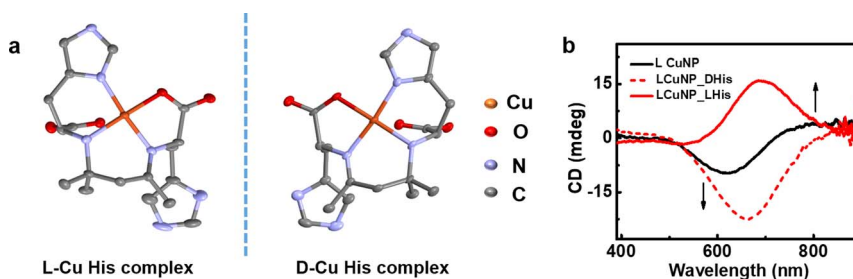

Fig. 5 (a) X-ray crystal structures of L- and D-copper-histidine complexes formed upon the addition of L- and D-histidine to L-CuNPs, respectively. (b) CD spectra of L-CuNPs before (black trace) and after the addition of histidine (red trace). Solid and dotted red lines correspond to spectra obtained after the addition of L- and D-histidine, respectively.

For the better understanding of ground-state photophysical activities, theoretical simulations were performed using Gaussian 09 software (Fig. S15–S17†). The calculations show absorption peaks at 686.36 nm and 350.79 nm involving energies of 1.8064 eV and 3.5345 eV, respectively. The simulated UV-visible and CD spectra of the metal complex match well with experimental plots confirming the structural purity of the complex as well as the nature of excitations (Fig. S16†). To study the reversibility of the process, cysteine was added to the formed complex. However, subsequent addition of cysteine to the complex showed the disappearance of CD signals but not the regaining of plasmonic peaks indicating that the conversion of nanoparticle to complex is an irreversible process (Fig. S18†). The relative binding strengths of cysteine and histidine to copper would act as the deciding factor for forward and reversible reactions, and these aspects were probed further.

Investigations of the mechanism show that the nanoparticle-to-complex conversion is facilitated by the ligand-induced dissolution process as illustrated in Fig. 6. The process involves the utilization of specific molecules or ligands, such as amino acids in this particular case, to guide and control the dissolution of nanoparticles, leading to the subsequent formation of a complex. The addition of a new ligand would displace the surface-bound ligand on the nanoparticles or stabilize intermediate surface species, promoting the release of ions into the surrounding medium. The ligand can then form a complex with released ions, stabilizing them in solution and preventing their re-adsorption onto the nanoparticle surface. The complex formation was further identified by the change in the morphology of the nanoparticles with histidine addition. The nanoparticle size decreased gradually with each successive addition of histidine leading to the absence of visible particles in SEM images following the last addition. These observations may be ascribed to the dissolution of nanoparticles and subsequent liberation of ions and complex formation (Fig. S19†). Ligands with a high binding affinity for the nanoparticle surface and those with the ability to promote redox reactions are more likely to induce dissolution.[60,61] The relative binding strengths of amino acids determine their ability to form stable complexes and control the dissolution process.

The spectral changes of the CuNPs upon treatment with different amino acids indicate that positively charged amino acids such as histidine and lysine interact well with the CuNPs (Fig. S12–S14†). In contrast, addition of L- and D-cysteine to L-CuNPs resulted in the complete loss of chirality due to the aggregation and precipitation of nanoparticles. The overall findings from amino acid addition experiments are that the binding is specific to histidine leading to a noticeable inversion of the CD signal. This outcome is attributed to the exceptional binding capability of histidine to copper, characterized by high binding constants. To substantiate this claim, binding constant values for the interaction of copper with various amino acids were calculated using the Benesi–Hildebrand method (Fig. S20†). The calculated values were found to be 5.43×10^7 M^{-1}, 1.37×10^4 M^{-1} and 2.33×10^5 M^{-1} for copper binding with histidine, cysteine and lysine, respectively. The irreversibility of the complex-to-nanoparticle conversion is also a result of this difference in binding strengths. The binding mechanism of histidine to copper differs from that of other amino acids primarily due to its distinctive imidazole side chain. The unshared electrons on the imidazole nitrogen atom enable the formation of coordination bonds with copper ions. This proposition was further supported by the SC-XRD analysis of the complex formed upon addition of histidine to L-CuNPs (vide supra). The observed inversion in CD signals with histidine, in contrast to other amino acids, can be attributed to the involvement of the imidazole group in bonding, resulting in an asymmetric distorted square planar geometry.

Conclusions

In summary, we have developed a facile strategy for the synthesis of CuNPs using cysteine as the chiral precursor and capping agent. The optically active nanoparticles showed distinct mirror image CD spectral profiles for the particles synthesized using opposite isomers of the capping ligand. The origin of chirality was theoretically validated to the interaction between the achiral particle and chiral ligand shell. The optically active nanoparticles could be used for selective detection as well as enantioselective recognition of histidine, an essential amino acid with biological significance. The interaction of histidine with CuNPs resulted in the nanoparticle-to-complex conversion through ligand-induced dissolution. The formation of the copper-histidine complex was marked by a reversal of the CD signal for one isomer of histidine, whereas an enhancement of signal for the opposite isomer enabled its enantioselective recognition. The selectivity of amino acid was governed by the presence of imidazole group of histidine that binds to copper to form a distorted square planar geometry. These findings significantly contribute to the understanding of the underlying mechanism behind the generation of chirality in nanoparticles. Moreover, deeper knowledge on specific interactions between chiral nanoparticles and biomolecules opens
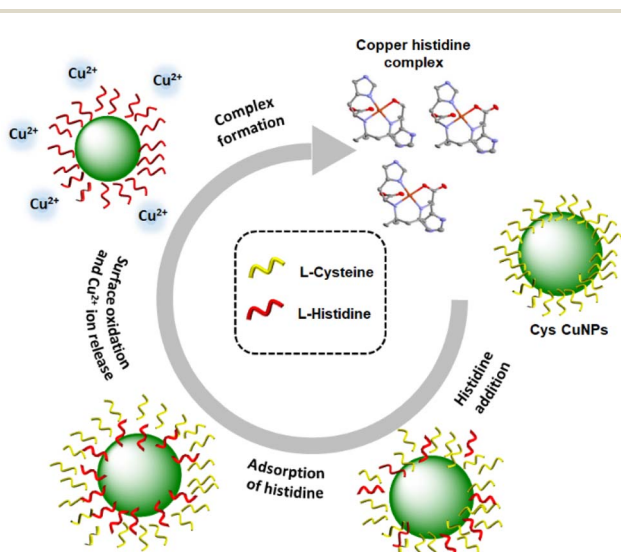

Fig. 6 Scheme illustrating the nanoparticle -to-complex conversion through the ligand-induced dissolution process.

new avenues for their diverse applications in areas such as biomedical diagnostics and asymmetric catalysis.

Data availability

All experimental details and supporting data are added to the ESI file.†

Author contributions

J. K. conceived and coordinated the project. S. M., C. D. and A. C. carried out the experiments. D. M. S. carried out the theoretical simulations. All authors analysed the data. S. M., D. M. S. and J. K. prepared the manuscript. All authors have given approval to the final version of the manuscript.

Conflicts of interest

There are no conflicts to declare.

Acknowledgements

Notes and references

1 A. Guerrero-Martínez, J. L. Alonso-Gómez, B. Auguié, M. Cid and L. M. Liz-Marzán, From individual to collective chirality in metal nanoparticles, *Nano Today*, 2011, **6**, 381–400.

2 W. Ma, L. Xu, A. F. de Moura, X. Wu, H. Kuang, C. Xu and N. A. Kotov, Chiral inorganic nanostructures, *Chem. Rev.*, 2017, **117**, 8041–8093.

3 L. A. Warning, A. R. Miandashti, L. A. McCarthy, Q. Zhang, C. F. Landes and S. Link, Nanophotonic approaches for chirality sensing, *ACS Nano*, 2021, **15**, 15538–15566.

4 C. Gautier and T. Bürgi, Chiral gold nanoparticles, *ChemPhysChem*, 2009, **10**, 483–492.

5 F. P. Milton, J. Govan, M. V. Mukhina and Y. K. Gun'ko, The chiral nano-world: chiroptically active quantum nanostructures, *Nanoscale Horiz.*, 2016, **1**, 14–26.

6 N. H. Cho, A. Guerrero-Martínez, J. Ma, S. Bals, N. A. Kotov, L. M. Liz-Marzán and K. T. Nam, Bioinspired chiral inorganic nanomaterials, *Nat. Rev. Bioeng.*, 2023, **1**, 88–106.

7 N. S. Nizar, M. Sujith, K. Swathi, C. Sissa, A. Painelli and K. G. Thomas, Emergent chiroptical properties in

8 J. Cheng, G. Le Saux, J. Gao, T. Buffeteau, Y. Battie, P. Barois, V. Ponsinet, M. H. Delville, O. Ersen, E. Pouget and R. Oda, GoldHelix: gold nanoparticles forming 3D helical superstructures with controlled morphology and strong chiroptical property, *ACS Nano*, 2017, **11**, 3806–3818.

9 T. Nakashima, Y. Kobayashi and T. Kawai, Optical activity and chiral memory of thiol-capped CdTe nanocrystals, *J. Am. Chem. Soc.*, 2009, **131**, 10342–10343.

10 A. Döring, E. Ushakova and A. L. Rogach, Chiral carbon dots: synthesis, optical properties, and emerging applications, *Light Sci. Appl.*, 2022, **11**, 75.

11 J. Kumar, K. G. Thomas and L. M. Liz-Marzán, Nanoscale chirality in metal and semiconductor nanoparticles, *Chem. Commun.*, 2016, **52**, 12555–12569.

12 C. Dutta, S. Maniappan and J. Kumar, Delayed luminescence guided enhanced circularly polarized emission in atomically precise copper nanoclusters, *Chem. Sci.*, 2023, **14**, 5593–5601.

13 S. Maniappan, K. L. Reddy and J. Kumar, Transmitting biomolecular chirality into carbon nanodots: a facile approach to acquire chiral light emission at the nanoscale, *Chem. Sci.*, 2023, **14**, 491–498.

14 M. V. Mukhina, V. G. Maslov, A. V. Baranov, A. V. Fedorov, A. O. Orlova, F. Purcell-Milton, J. Govan and Y. K. Gun'ko, Intrinsic chirality of CdSe/ZnS quantum dots and quantum rods, *Nano Lett.*, 2015, **15**, 2844–2851.

15 X. Yang, J. Lv, J. Zhang, T. Shen, T. Xing, F. Qi, S. Ma, X. Gao, W. Zhang and Z. Tang, Tunable circularly polarized luminescence from inorganic chiral photonic crystals doped with quantum dots, *Angew. Chem., Int. Ed.*, 2022, **61**, e202201674.

16 K. L. Reddy, J. P. Mathew, S. Maniappan, C. Tom, E. Shiby, R. K. Pujala and J. Kumar, Mandelic acid appended chiral gels as efficient templates for multicolour circularly polarized luminescence, *Nanoscale*, 2022, **14**, 4946–4956.

17 R. Thomas, J. Kumar, R. S. Swathi and K. G. Thomas, Optical Effects Near Metal Nanostructures: Towards Surface-enhanced Spectroscopy, *Curr. Sci.*, 2012, **102**, 85–96.

18 E. S. Goerlitzer, A. S. Puri, J. J. Moses, L. V. Poulikakos and N. Vogel, The Beginner's Guide to Chiral Plasmonics: Mostly Harmless Theory and the Design of Large-Area Substrates, *Adv. Opt. Mater.*, 2021, **9**, 2100378.

19 Y. Luo, C. Chi, M. Jiang, R. Li, S. Zu, Y. Li and Z. Fang, Plasmonic chiral nanostructures: chiroptical effects and applications, *Adv. Opt. Mater.*, 2017, **5**, 1700040.

20 H. Chen, L. Shao, Q. Li and J. Wang, Gold nanorods and their plasmonic properties, *Chem. Soc. Rev.*, 2013, **42**, 2679–2724.

21 J. Krajczewski, K. Kołątaj and A. Kudelski, Plasmonic nanoparticles in chemical analysis, *RSC Adv.*, 2017, **7**, 17559–17576.

22 S. Maniappan, C. Dutta, D. M. Solís, J. M. Taboada and J. Kumar, Surfactant directed synthesis of intrinsically chiral plasmonic nanostructures and precise tuning of

supramolecular and plasmonic assemblies, *Chem. Soc. Rev.*, 2021, **50**, 11208–11226.

their optical activity through controlled self-assembly, *Angew. Chem., Int. Ed.*, 2023, **62**, e202300461.

23 D. Vila-Liarte, N. A. Kotov and L. M. Liz-Marzán, Template-assisted self-assembly of achiral plasmonic nanoparticles into chiral structures, *Chem. Sci.*, 2022, **13**, 595–610.

24 A. Kuzyk, R. Schreiber, Z. Fan, G. Pardatscher, E. M. Roller, A. Högele, F. C. Simmel, A. O. Govorov and T. Liedl, DNA-based self-assembly of chiral plasmonic nanostructures with tailored optical response, *Nature*, 2012, **483**, 311–314.

25 W. Wu and M. Pauly, Chiral plasmonic nanostructures: recent advances in their synthesis and applications, *Mater. Adv.*, 2022, **3**, 186–215.

26 G. Shemer, O. Krichevski, G. Markovich, T. Molotsky, I. Lubitz and A. B. Kotlyar, Chirality of silver nanoparticles synthesized on DNA, *J. Am. Chem. Soc.*, 2006, **128**, 11006–11007.

27 N. Kowalska, F. Bandalewicz, J. Kowalski, S. Gómez-Graña, M. Bagiński, I. Pastoriza-Santos, M. Grzelczak, J. Matraszek, J. Pérez-Juste and W. Lewandowski, Hydrophobic gold nanoparticles with intrinsic chirality for the efficient fabrication of chiral plasmonic nanocomposites, *ACS Appl. Mater. Interfaces*, 2022, **14**, 50013–50023.

28 M. B. Gawande, A. Goswami, F. X. Felpin, T. Asefa, X. Huang, R. Silva, X. Zou, R. Zboril and R. S. Varma, Cu and Cu-based nanoparticles: synthesis and applications in catalysis, *Chem. Rev.*, 2016, **116**, 3722–3811.

29 F. Parveen, B. Sannakki, M. V. Mandke and H. M. Pathan, Copper nanoparticles: Synthesis methods and its light harvesting performance, *Sol. Energy Mater. Sol. Cells*, 2016, **144**, 371–382.

30 Q. C. Sun, Y. Ding, S. M. Goodman, H. H. Funke and P. Nagpal, Copper plasmonics and catalysis: role of electron–phonon interactions in dephasing localized surface plasmons, *Nanoscale*, 2014, **6**, 12450–12457.

31 Z. Lyu, Y. Shang and Y. Xia, Shape-controlled synthesis of copper nanocrystals for plasmonic, biomedical, and electrocatalytic applications, *Acc. Chem. Res.*, 2022, **3**, 1137–1148.

32 T. Zhao, D. Meng, Z. Hu, W. Sun, Y. Ji, J. Han, X. Jin, X. Wu and P. Duan, Enhanced chiroptical properties of nanocomposites of achiral plasmonic nanoparticles decorated with chiral dye-loaded micelles, *Nat. Commun.*, 2023, **14**, 81.

33 A. V. Markin and N. E. Markina, Experimenting with plasmonic copper nanoparticles to demonstrate color changes and reactivity at the nanoscale, *J. Chem. Educ.*, 2019, **96**, 1438–1442.

34 N. Verma and N. Kumar, Synthesis and biomedical applications of copper oxide nanoparticles: an expanding horizon, *ACS Biomater. Sci. Eng.*, 2019, **5**, 1170–1188.

35 L. Tang, L. Zhu, F. Tang, C. Yao, J. Wang and L. Li, Mild synthesis of copper nanoparticles with enhanced oxidative stability and their application in antibacterial films, *Langmuir*, 2018, **34**, 14570–14576.

36 M. E. Villanueva, A. M. D. R. Diez, J. A. Gonzalez, C. J. Pérez, M. Orrego, L. Piehl, S. Teves and G. J. Copello, Antimicrobial

37 Y. Gu, W. Wang, C. Gao, L. Feng, J. Wu and L. Zhao, Chiral CuS nanoparticles and their photothermal properties, *CrystEngComm*, 2022, **24**, 4955–4961.

activity of starch hydrogel incorporated with copper nanoparticles, *ACS Appl. Mater. Interfaces*, 2016, **8**, 16280–16288.

38 Y. Duan, X. Liu, L. Han, S. Asahina, D. Xu, Y. Cao, Y. Yao and S. Che, Optically active chiral CuO "nanoflowers", *J. Am. Chem. Soc.*, 2014, **136**, 7193–7196.

39 Q. Ma, C. Cheng, D. Luo, J. Qiao and L. Qi, Dipeptide-capped copper nanoparticles as chiral nanozymes for colorimetric enantioselective recognition of 3,4-dihydroxy-D-, L-phenylalanine, *ACS Appl. Bio Mater.*, 2023, **6**, 1676–1682.

40 C. Hao, A. Qu, L. Xu, M. Sun, H. Zhang, C. Xu and H. Kuang, Chiral molecule-mediated porous Cu_xO nanoparticle clusters with antioxidation activity for ameliorating Parkinson's disease, *J. Am. Chem. Soc.*, 2018, **141**, 1091–1099.

41 S. Bettini, N. Grover, M. Ottolini, C. Mattern, L. Valli, M. O. Senge and G. Giancane, Enantioselective discrimination of histidine by means of an achiral cubane-bridged bis-porphyrin, *Langmuir*, 2021, **37**, 13882–13889.

42 Y. Mao, M. A. Abed, N. B. Lee, X. Wu, G. Du and L. Pu, Determining the concentration and enantiomeric composition of histidine using one fluorescent probe, *Chem. Commun.*, 2021, **57**, 587–590.

43 M. Markert, U. Scheffler and R. Mahrwald, Asymmetric histidine-catalyzed cross-aldol reactions of enolizable aldehydes: access to defined configured quaternary stereogenic centers, *J. Am. Chem. Soc.*, 2009, **131**, 16642–16643.

44 R. I. Stefan-van Staden, Enantioanalysis of D-histidine based on its interaction with [5,6]fullerene-C_{70} and diethyl(1, 2-methanofullerene-C_{70})-71,71-dicarboxylate, *New J. Chem.*, 2010, **34**, 1141–1147.

45 B. Ma, S. Wang, F. Liu, S. Zhang, J. Duan, Z. Li, Y. Kong, Y. Sang, H. Liu, W. Bu and L. Li, Self-assembled copper–amino acid nanoparticles for *in situ* glutathione "AND" H_2O_2 sequentially triggered chemodynamic therapy, *J. Am. Chem. Soc.*, 2018, **141**, 849–857.

46 Y. Imanaka, T. Nakahodo and H. Fujihara, Chiral copper (0) nanoparticles: direct synthesis and interfacial chiral induction *via* phase transfer of copper nanoparticles, *ChemistrySelect*, 2017, **2**, 5806–5809.

47 M. Raja, J. Subha, F. B. Ali and S. H. Ryu, Synthesis of copper nanoparticles by electroreduction process, *Mater. Manuf. Processes*, 2008, **23**, 782–785.

48 P. Liu, Z. Li, W. Cai, M. Fang and X. Luo, Fabrication of cuprous oxide nanoparticles by laser ablation in PVP aqueous solution, *RSC Adv.*, 2011, **1**, 847–851.

49 N. Kumar and L. S. B. Upadhyay, Facile and green synthesis of highly stable L-cysteine functionalized copper nanoparticles, *Appl. Surf. Sci.*, 2016, **385**, 225–233.

50 Y. Xie, G. Bertoni, A. Riedinger, A. Sathya, M. Prato, S. Marras, R. Tu, T. Pellegrino and L. Manna, Nanoscale transformations in covellite (CuS) nanocrystals in the presence of divalent metal cations in a mild reducing environment, *Chem. Mater.*, 2015, **27**, 7531–7537.

51 N. T. T. Mai, M. M. Neto, P. Van Thang, N. N. Trung, N. C. Tu, T. N. Dung, H. D. Chinh and L. T. L. Anh, Cu$_2$O nanoparticles: A simple synthesis, characterization and its photocatalytic performance toward methylene blue, *Mat. Transact.*, 2020, **61**, 1868–1873.

52 A. O. Govorov, Z. Fan, P. Hernandez, J. M. Slocik and R. R. Naik, Theory of circular dichroism of nanomaterials comprising chiral molecules and nanocrystals: plasmon enhancement, dipole interactions, and dielectric effects, *Nano Lett.*, 2010, **10**, 1374–1382.

53 E. Csapó, R. Patakfalvi, V. Hornok, L. T. Tóth, A. Sipos, A. Szalai, M. Csete and I. Dékány, Effect of pH on stability and plasmonic properties of cysteine-functionalized silver nanoparticle dispersion, *Colloids Surf., B*, 2012, **98**, 43–49.

54 S. Devi, B. Singh, A. K. Paul and S. Tyagi, Highly sensitive and selective detection of trinitrotoluene using cysteine-capped gold nanoparticles, *Anal. Methods*, 2016, **8**, 4398–4405.

55 C. F. Bohren and D. R. Huffman, *Absorption and scattering of light by small particles*, John Wiley & Sons, 2008.

56 G. Zheng, Z. Bao, J. Pérez-Juste, R. Du, W. Liu, J. Dai, W. Zhang, L. Y. S. Lee and K. Y. Wong, Tuning the morphology and chiroptical properties of discrete gold nanorods with amino acids, *Angew. Chem., Int. Ed.*, 2018, **57**, 16452–16457.

57 P. B. Johnson and R. W. Christy, Optical constants of the noble metals, *Phys. Rev. B*, 1972, **6**, 4370.

58 P. Deschamps, P. P. Kulkarni and B. Sarkar, *Inorg. Chem.*, 2003, **42**, 7366–7368.

59 J. Mesu, T. Visser, F. Soulimani, E. E. van Faassen, P. de Peinder, A. M. Beale and B. M. Weckhuysen, New insights into the coordination chemistry and molecular structure of copper(II) histidine complexes in aqueous solutions, *Inorg. Chem.*, 2006, **45**, 1960–1971.

60 R. D. Kent and P. J. Vikesland, Dissolution and persistence of copper-based nanomaterials in undersaturated solutions with respect to cupric solid phases, *Environ. Sci. Technol.*, 2016, **50**, 6772–6781.

61 L. F. Wang, N. Habibul, D. Q. He, W. W. Li, X. Zhang, H. Jiang and H. Q. Yu, Copper release from copper nanoparticles in the presence of natural organic matter, *Water Res.*, 2015, **68**, 12–23.